Topological insulator Bi_2Se_3(111) surface doped with transition metals: An *ab initio* investigation

L. B. Abdalla,[1,*] L. Seixas,[1] T. M. Schmidt,[2] R. H. Miwa,[2,†] and A. Fazzio[1]
[1]*Instituto de Física, Universidade de São Paulo, São Paulo, SP, Brazil*
[2]*Instituto de Física, Universidade Federal de Uberlândia, 38400-902 Uberlândia, MG, Brazil*
(Received 16 April 2013; published 15 July 2013)

Based on first-principles calculations, we provide a map of the energetic stability and the electronic behavior of the topologically protected surface states of the topological insulator (TI), Bi_2Se_3, doped with transition metals (TMs), TM/Bi_2Se_3(111). We find that Fe, Mn, and Cr impurities are energetically more stable at the Bi substitutional sites, whereas we may find energetically stable substitutional as well as interstitial configurations for Co and Ni impurity atoms. Through scanning tunneling microscopy simulations, we verify that each TM atomic species and its position in the Bi_2Se_3(111) surface can be identified. The substitutional Fe and Cr impurities exhibit an energetic preference for the out-of-plane net magnetic moment, giving rise to a small energy gap at the Dirac point (DP), whereas the in-plane magnetic moment of substitutional Mn/Bi_2Se_3(111) promotes a shift of the DP from the center of the surface Brillouin zone, opening up a small energy gap. For the substitutional impurities, the shapes of the metallic bands are somewhat preserved compared with the energy bands of the pristine Bi_2Se_3(111) surface. Interstitial Co atoms also present an in-plane net magnetic moment, where we find the formation of metallic bands, suppressing the presence of the DP. For the Ni/Bi_2Se_3(111) impurity there is not a net magnetic moment, and therefore, the DP is preserved. Further formation energy results indicate other plausible (meta)stable impurity configurations, giving rise to quite different scenarios for the topological properties of TM/Bi_2Se_3(111), even for the same TM impurity.

DOI: 10.1103/PhysRevB.88.045312 PACS number(s): 73.20.Hb, 73.20.At

I. INTRODUCTION

Topological insulators (TIs) have attracted a lot of attention in condensed matters physics and material science. These materials exhibit a gap inversion in their bulk phase, generated by a strong spin-orbit coupling, and topologically protected metallic states at the trivial/topological (interface) contact region.[1] Metallic states have their spin polarization locked in a plane creating a chiral texture, similar to the quantum spin hall, which, by destructive interference of the wave function, suppresses all kind of backscattering processes. They are protected against any time-reversal-invariant perturbation, because of the topological order described by the Z_2 invariant.[2–6]

In 2006, Bernevig *et al.* proposed a TI phase in the HgTe/CdTe heterostructure,[7] and one year later such a two-dimensional (2D) TI structure was successfully built up.[8] In these systems, the band gap inversion is ruled by the width of the HgTe quantum well. Further investigations have pointed out that the R_{3m} rhombohedral crystal family, like Bi_2Se_3 and Bi_2Te_3, also exhibits such an exotic electronic phase, the so-called 3D TIs.[9,10] The topologically protected metallic states lie at the trivial/topological contact region, namely, in these 3D TIs we will have topological surface states (TSSs). For instance, on the (111) surface of Bi_2Se_3, the TSS exhibits a single Dirac cone at the center of the Brillouin zone ($\bar{\Gamma}$ point), while in its bulk phase, Bi_2Se_3 presents an (inverted) energy gap of $\sim$300 meV. Indeed, Bi_2Se_3 has been considered a very promising TI material for electronic and spintronic applications.[9–12] Several applications of TIs rely on doping processes, like the incorporation of magnetic impurities.

Upon the presence of an external magnetic field, the time-reversal symmetry (TRS) has been removed, opening an energy gap at the Dirac point (DP) and giving rise to massive Dirac fermions. The Kramers degeneracy is no longer valid, and backscattering processes become allowed. Magnetic impurities embedded in 3D TIs surface will play the same role as the external magnetic field. The interaction between the magnetic impurities and the TI (host) surface is an important issue to be addressed, since the local hybridization between the impurity atom and the host surface will rule the electronic structure of the TSSs. Great effort has been made in this direction: for instance, (i) scanning tunneling microscopy (STM) images[13–16] and core-level spectroscopy results[17] have been used to identify the geometry of the impurity atoms near the TI surface region; and meanwhile, (ii) the electronic structure of the TSS has been characterized through angle-resolved photoemission spectroscopy (ARPES) experiments. However, we find a number of contradictory results for both i and ii. For instance, an energy gap at the DP has been verified for Fe and Mn magnetic impurities,[16,18–20] while in Refs. 17 and 21 the authors state that the DP has been preserved for magnetic impurities such as Gd and Fe in TI Bi_2Se_3(111) surfaces. However, in Refs. 13, 14, 16, 22, and 23, we find quite controversial results regarding the equilibrium configurations of impurity atoms in TIs.

A previous theoretical study, based on effective Hamiltonian models,[24] indicates that the lifting of the $\bar{\Gamma}$-point degeneracy is due to the net magnetization perpendicular to the surface (out of plane). Further first-principles calculations, mostly based on the density functional theory (DFT), support the presence of an energy gap at the DP, as well as the suppression of the TRS, mediated by the presence of an out-of-plane magnetic moment induced by the impurities lying on the TI surface.[25–29] On the other hand, there are theoretical studies, based on the same calculation approach, indicating an in-plane magnetization merely shifting the Dirac cone from the center of the Brillouin zone.[30,31]

In this work we have performed a systematic investigation of Bi_2Se_3(111) TI doped with transition metals (TMs),

TM/Bi_2Se_3(111). Through *ab initio* total energy calculation we present a detailed map of the energetic stability of TMs embedded in Bi_2Se_3(111). Changes in the surface electronic charge density were examined through STM simulations and compared with the (available) experimental STM pictures. Our electronic structure calculations reveal that, indeed, the TSSs present a strong dependence on the configuration (hybridization) of the TMs in Bi_2Se_3(111). For the energetically more likely substitutional TM/Bi_2Se_3(111) systems (TM = Fe, Mn, and Cr), the TSSs are weakly perturbed due to the presence of the magnetic impurity. For Fe and Cr, there is a small energy gap for the out-of-plane net magnetic moment, while the DP is shifted from the center of the Brillouin zone due to the in-plane net magnetic moment (TM = Mn). For both scenarios, the TRS was broken. We have also examined the interstitial and surface adsorbed configurations. The former configuration is quite likely for Co and Ni impurities. In this case, there is an energy gap for interstitial Co impurities, while for Ni impurities we find zero net magnetic moment, preserving the DP and the TRS. Aiming to provide a more complete picture of TM/Bi_2Se_3(111), we have examined not only the energetically most stable TM/Bi_2Se_3(111) systems, but also the ones proposed in previous studies as well as those with lower formation energies.

II. METHOD

The calculations were performed within the DFT,[32,33] by using the pseudopotential method, with projected augmented wave potentials,[34,35] to describe electron-ion interactions. The exchange-correlation functional was calculated within the Perdew-Burke-Ernzenhof generalized gradient approximation,[36] as implemented in the Vienna Ab Initio Simulation Package.[37] The Kohn-Sham orbitals are expanded in a plane-wave basis set with an energy cutoff of 270 eV. The Brillouin zone was sampled by a Γ center scheme, by using a number of **k** points up to $2 \times 2 \times 1$ including the $\bar{\Gamma}$ point, such that the total energy was converged. Bi_2Se_3 has a rhombohedral crystal structure, where the five atoms forming the unit cell belong to three inequivalent quintuple layers. In this work we have used a supercell with a hexagonal lattice structure in order to simulate the Bi_2Se_3(111) surface. A slab method was used with a vacuum layer of at least 20 Å to avoid interaction between adjacent surfaces. Our unit cell has four quintuple layers, in order to describe properly the surface massless Dirac cone,[38] and a 3×3 surface periodicity which corresponds to a TM doping of around 10%. The topmost four layers including the impurity (TM) atom are allowed to relax, until the atomic forces are smaller than 10 meV/Å.

The TM/Bi_2Se_3(111) formation energy was calculated according to[39]

$$E^F = E[\mathrm{TM/Bi_2Se_3(111)}] - E[\mathrm{Bi_2Se_3(111)}] + n\mu_{\mathrm{Bi/Se}} - \mu_{\mathrm{TM}},$$

where E[TM/Bi_2Se_3(111)] and E[Bi_2Se_3(111)] are the total energies of the slab with and without the TM impurity, respectively, and n can be either 1 for substitutional or 0 for interstitial/adsorbed TM configurations. $\mu_{\mathrm{Bi/Se}}$ and μ_{TM} are the total energy per atom of the respective bulk phase, $\mu^{\mathrm{bulk}}_{\mathrm{Bi/Se}}$ and $\mu^{\mathrm{bulk}}_{\mathrm{TM}}$. The accuracy of our calculated chemical potentials was verified through the calculation of the cohesive energies of the respective bulk (elemental) phases[40] and compared with previous works.[41,42] Since we are considering $\mu_{\mathrm{Bi}} = \mu^{\mathrm{max}}_{\mathrm{Bi}} = \mu^{\mathrm{bulk}}_{\mathrm{Bi}}$ ($\mu_{\mathrm{Se}} = \mu^{\mathrm{max}}_{\mathrm{Se}} = \mu^{\mathrm{bulk}}_{\mathrm{Se}}$), the formation energies for the substitutional impurities were obtained under the Bi-rich (Se-rich) condition, whereas for the Bi-poor (Se-poor) condition we have $\mu_{\mathrm{Bi}} = \mu^{\mathrm{min}}_{\mathrm{Bi}} = \mu^{\mathrm{bulk}}_{\mathrm{Bi}} - \Delta H_{\mathrm{Bi_2Se_3}}/2$ ($\mu_{\mathrm{Se}} = \mu^{\mathrm{min}}_{\mathrm{Se}} = \mu^{\mathrm{bulk}}_{\mathrm{Se}} - \Delta H_{\mathrm{Bi_2Se_3}}/3$). Our calculated formation enthalpy, $\Delta H_{\mathrm{Bi_2Se_3}} = 1.37$ eV, is very close to the recent experimental measurement, 1.50 eV.[43] STM calculations, based on the Tersoff-Hamann scheme,[44] were obtained at a constant height mode, at about 2 Å (1 Å) from the topmost atom for all doped (pristine) cases. We used the R-G-B (red-green-blue) gradient of color, where dark blue represents the absence of charge and the saturation color varies in each system in order to see the subtle variations of the local charge density. The electronic band structures were analyzed following the procedure proposed by Park *et al.*,[45] by considering a critical percentage of 10% for the (single-particle) wave function projected onto the topmost two monolayers of the Bi_2Se_3(111) slab.

III. RESULTS AND COMMENTS

A. Pristine Bi_2Se_3(111)

Figure 1 presents the structural model of the pristine Se-terminated Bi_2Se_3(111) surface. At the equilibrium geometry we verify that (i) there is no surface reconstruction, namely, the surface exhibits a (1×1) periodicity, while (ii) the topmost Se (Bi) atom exhibits a vertical inward (outward) displacement of 0.15 (0.03) Å. In this case, the topmost Bi-Se bonds are compressed by 0.10 Å (2.97 → 2.87 Å). Our simulated STM images show the formation of bright spots lying on the topmost Se atoms [Fig. 2(a)], confirming the (1×1) surface periodicity and in accordance with previous experimental and theoretical findings.[46,47]

TIs in contact with nontopological (trivial) insulators promote the formation of topologically protected metallic states in the (trivial/topological) interface region.[1] In particular, for the Bi_2Se_3(111)–(1×1) surface we will have topologically protected metallic states for wave vectors parallel to the (111) surface plane, so-called TSSs. Figure 2(b) presents the

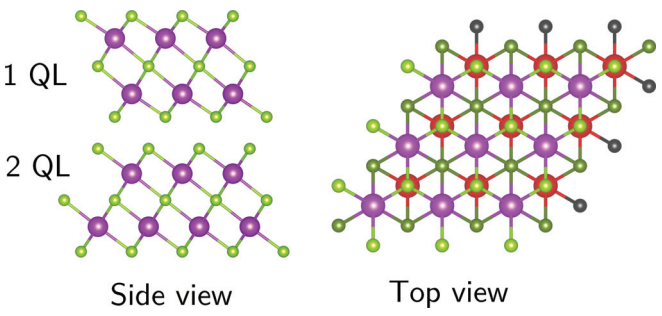

FIG. 1. (Color online) Structural model of the pristine Bi_2Se_3 system. In the top view we use different colors as a guide for the eye, where light green, dark green, black, violet, and red represent, respectively, the first Se, second Se, third Se, first Bi, and second Bi monolayers, respectively. QL, quintuple layer.

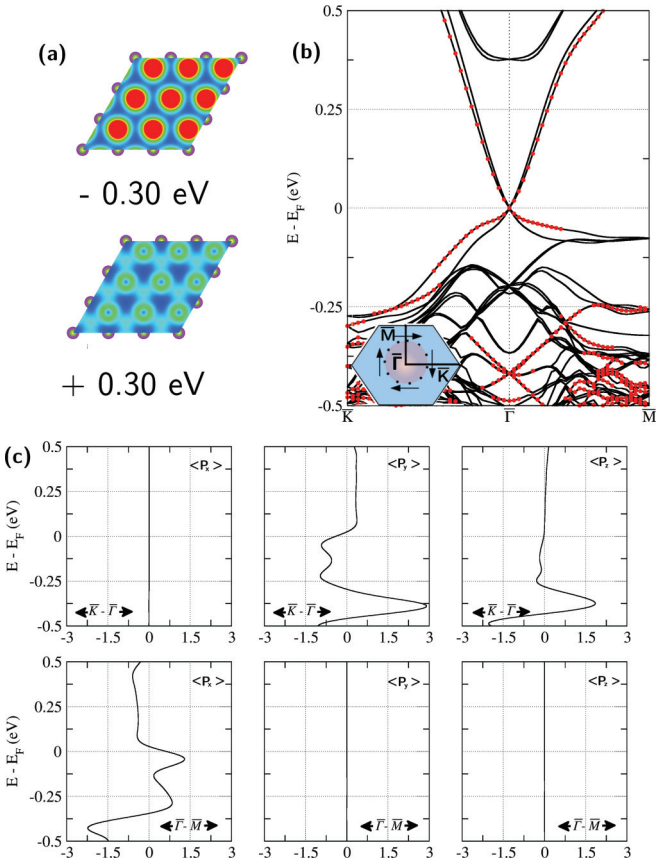

FIG. 2. (Color online) Key electronic properties of the pristine Bi_2Se_3 surface: (a) STM images for the occupied (top) and empty (bottom) states, (b) electronic band structure along the $\bar{K}\bar{\Gamma}\bar{M}$ direction, and (c) spin-projected density of states, $P_\alpha(E)$, along the $\bar{\Gamma}$–$\bar{K}$ (top) and $\bar{\Gamma}$–$\bar{M}$ (bottom) directions. In (b), solid (black) lines indicate the contribution of the whole Bi_2Se_3(111) slab, and (red) circles indicate the electronic contributions of the topmost two MLs. Those contributions were selected by considering a critical percentage (larger than 10%) for the single-particle wave functions of the topmost two MLs. Inset in (b): Schematic of the helical spin texture for occupied states near the Fermi level.

electronic band structure of the Bi_2Se_3(111)–(1 × 1) surface, where we verify the formation of a Dirac-like cone located at the $\bar{\Gamma}$ point. Since the space inversion symmetry is broken at the surface, the TSSs are (spin) split by the spin-orbit interaction, Rashba-Bychkov effect.[48] Meanwhile the TRS has been preserved, $E(\mathbf{k},\uparrow) = E(-\mathbf{k},\downarrow)$. In accordance with the maintenance of the TRS and the Rashba-Bychkov band splitting of the surface states, spin polarization vectors ($\langle\mathbf{S}\rangle$) of opposite momentum ($\mathbf{k}$) should have opposite signs, $\langle\mathbf{S}_n(\mathbf{k})\rangle = -\langle\mathbf{S}_n(-\mathbf{k})\rangle$, for a given energy band n, with $\langle\mathbf{S}\rangle$ perpendicularly locked to the surface wave vector $\mathbf{k}$.[49] That is, TSS will present a helical spin texture.[11] Here, the spin-polarization vector can be written in terms of its Cartesian components, $\langle S_{n,\alpha}(\mathbf{k})\rangle = (\hbar/2)\langle\varphi_n(\mathbf{k})|\sigma_\alpha|\varphi_n(\mathbf{k})\rangle$ ($\alpha = x,y,z$), σ_α represents the Pauli matrices, and $\varphi_n(\mathbf{k})$ is the single-particle Kohn-Sham eigenfunction. Figure 2(c) presents the calculated energy-resolved spin-projected density of states (SPDOS), where for each Cartesian component of $\langle\mathbf{S}\rangle$, the SPDOS is defined as $P_\alpha(E) = \sum_{n,\mathbf{k}}\langle S_{n,\alpha}(\mathbf{k})\rangle\delta(E - E_n(\mathbf{k}))$. In agreement with the helical spin texture, near the Fermi level, in Fig. 2(c) we find that (i) for wave vectors parallel to the $\bar{\Gamma}$–$\bar{K}$ direction we have $P_x(E) = 0$, and (ii) $P_y(E) = 0$ for $\mathbf{k}$ along the $\bar{\Gamma}$–$\bar{M}$ direction. On the other hand, near the Dirac point, (iii) for $\mathbf{k}$ parallel to $\bar{\Gamma}$–$\bar{K}$, $P_y(E)$ presents negative (positive) values for occupied (empty) states, whereas (iv) along the $\bar{\Gamma}$–$\bar{M}$ direction, $P_x(E)$ is positive (negative) for occupied (empty) states. In addition, the formation of a helical spin texture for $\langle\mathbf{S}_{n,x}\rangle$ and $\langle\mathbf{S}_{n,y}\rangle$ composed of surface states resonant within the Bi_2Se_3 bulk valence band is noteworthy. Finally, there is an out-of-plane component ($P_z(E)$) for wave vector $\mathbf{k}$ parallel to the $\bar{\Gamma}$–$\bar{K}$ direction, while it vanishes along the $\bar{\Gamma}$–$\bar{M}$ direction. The inset in Fig. 2(b) presents a schematic of the helical spin texture, described above, for the occupied electronic states near the Fermi level.

B. Structural properties of TM/Bi_2Se_3(111)

Now that the structural and electronic properties of the Bi_2Se_3(111) surface have been benchmarked with previous experimental[11,50] and theoretical[38] results, let us start our investigation of Bi_2Se_3(111) incorporated by TMs. Here we have examined the following TMs: Cr, Mn, Fe, Co, and Ni embedded in the Bi_2Se_3(111) surface. As depicted in Fig. 3, we have considered a number of plausible (substitutional, interstitial, and adsorbed) configurations of TMs within the first quintuple layer of the surface. The most likely configurations were inferred based on the calculation of the formation energy (E^F) as described in Sec. II. Our results of E^F are summarized in Table I.

Several studies have been done addressing magnetic impurities in TIs. Among these (currently) iron, followed by manganese, in Bi_2Se_3(111), have been the most studied. However, the experimental as well as the theoretical findings are far from being consensual. We start with iron impurities.

Iron-doped Bi_2Se_3(111), Fe/Bi_2Se_3(111), exhibits an energetic preference for the substitutional Bi-sub configuration (Fe_{Bi}), $E^F = 1.05$ eV under the Bi-rich condition ($\mu_{Bi} = \mu_{Bi}^{max}$), whereas under the Bi-poor condition ($\mu_{Bi} = \mu_{Bi}^{min}$) the formation of Fe_{Bi} becomes more likely, where we obtained $E^F = 0.37$ eV. The substitutional Fe_{Bi} atom is sixfold

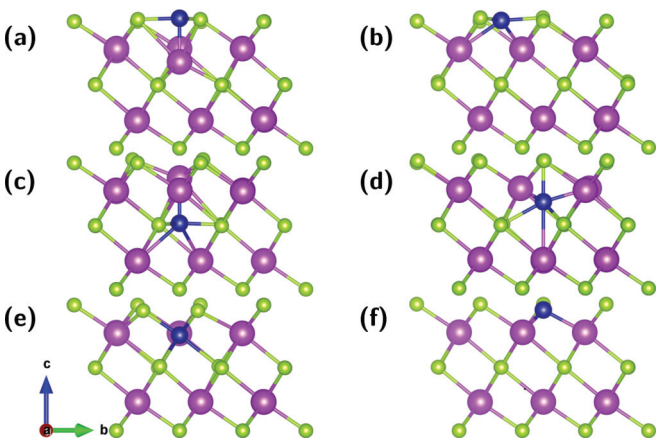

FIG. 3. (Color online) Structural models for the TM/Bi_2Se_3(111) surface: (a) Bi-ads, (b) Se-ads, (c) Bi-int,(d) Se-int, (e) Bi-sub. (f) and Se-sub.

TABLE I. Formation energies (in eV) of substitutional (sub; under the Bi-rich condition), interstitial (int), and adsorbed (ads) TM impurities in Bi_2Se_3(111).

Configuration	Cr	Mn	Fe	Co	Ni
Bi-sub	−0.10	0.04	1.05	1.69	1.33
Se-sub	3.34	2.96	3.58	3.44	2.33
Bi-int	1.14	0.46	1.17	1.14	0.63
Se-int	2.09	0.88	1.40	1.43	0.85
Bi-ads	1.36	0.74	1.28	1.30	0.75
Se-ads	2.49	0.87	1.40	1.35	0.68

TABLE II. Equilibrium geometry of the substitutional TM, Bi-sub configuration, detailed in Fig. 4. Atomic distances (d and h) are in Å, and bond angles (α) are in degrees.

TM	d^1	d^2	α^1	α^2	α^3	h
Pristine	2.87	3.10	92.32	91.80	83.76	1.59
Fe	2.54	2.82	90.90	91.41	86.19	1.44
Mn	2.60	2.70	86.57	91.78	89.82	1.59
Cr	2.54	2.65	86.17	91.54	90.66	1.56
Co	2.49	2.84	92.08	91.03	85.69	1.39
Ni	2.50	2.61	85.36	91.51	91.47	1.55

coordinated, forming three Fe-Se bonds with the topmost Se atoms and another three Fe-Se bonds with the third-layer Se atoms, as depicted in Figs. 4(a) and 4(b). The equilibrium geometries of the Bi-sub impurities are summarized in Table II. There is a local octahedral geometry around the impurity atom. At the equilibrium geometry, we find Fe-Se bond lengths (d_{FeSe}) of 2.54 and 2.82 Å, respectively. The formation of Fe_{Bi} is in good agreement with recent studies of TMs in Bi_2Se_3[23,51] and Fe-doped Bi_2Te_3(111).[52] The interstitial Bi-int configuration [Figs. 4(c) and 4(d)] is the second most likely structure with $E^F = 1.17$ eV. The interstitial Fe atom becomes sevenfold coordinated, forming three Fe-Se bonds, with $d_{FeSe} = 2.40$ Å (d^3), three Fe-Bi bonds ($d^2 = 3.26$ Å), and a Fe-Bi bond parallel to the [111] direction. In this case, the host Bi atom (of the second ML) exhibits an upward displacement of 0.89 Å perpendicularly to the surface plane, giving rise to a $(Fe\text{-}Bi)_{split}$-like structure with $d_{FeBi} = 2.40$ Å, indicated as d^1 in Fig. 4(d). The vertical distance

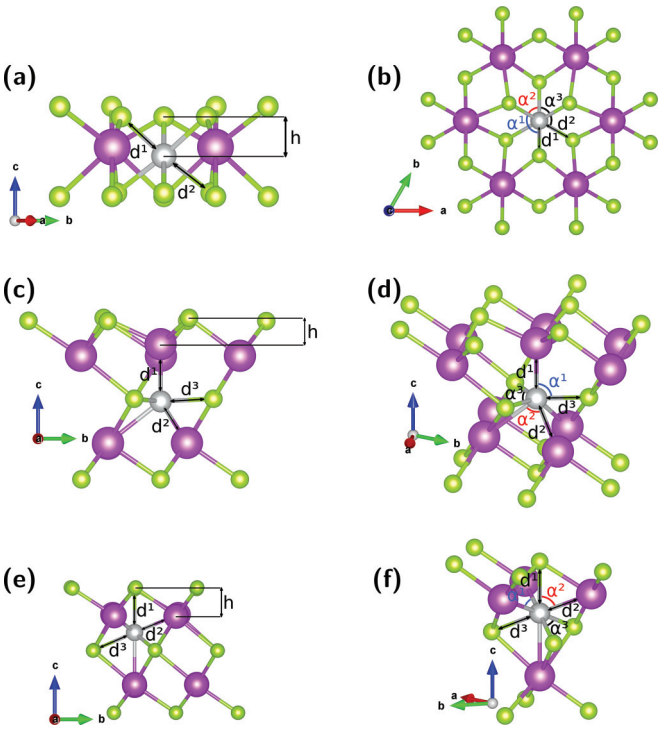

FIG. 4. (Color online) Structural model for the substitutional Bi-sub configuration side view (a) and top view (b), interstitial Bi-int side view (c), (d), and Se-int side view (e), (f).

h reduces from 1.59 Å [pristine Bi_2Se_3(111)] to 0.92 Å. The equilibrium geometries of interstitial TM/Bi_2Se_3(111) structures are detailed in Figs. 4(c)–4(f) and summarized in Table III.

Very recently, two different (metastable) geometries have been considered as good candidates for the Fe adsorbed Bi_2Se_3(111) surface, namely, Bi-ads and Se-ads, detailed in Figs. 5(a)–5(d), respectively. However, even for these two possible configurations, there are no conclusive results in the literature; *viz.*, in Ref. 30 the authors obtained a slight energetic preference (by 70 meV) for Se-ads. In contrast, Li *et al.*,[25] using a calculation approach similar to that used in Ref. 30, obtained an energetic preference of 75 meV for the Bi-ads structure. The latter result is in qualitative agreement with our findings, i.e., Bi-ads is more likely than Se-ads by 120 meV (see Table I). Further core-level spectroscopy studies provide a comprehensive picture for Fe adatoms on Bi_2Se_3(111).[17] The authors proposed two different environments, as a function of the deposition temperature, for Fe impurities in Bi_2Se_3(111). They find a Bi-5d core-level shift attributed to the chemical interaction between Fe adatoms and the Bi_2Se_3(111) surface, such a Bi-5d energy shift being more intense when the Fe impurities are deposited at room temperature, whereas such an energy shift decreases by around 20% for Fe deposition at low temperatures. The presence of different environments can be identified by the formation of Fe-Bi and Fe-Se chemical bonds. Our results indicate the presence of both Fe-Bi and Fe-Se bonds for the Bi-ads and Bi-int configurations. In the latter

TABLE III. Equilibrium geometry of the interstitial TM, Bi-sub, and Se-int configurations, detailed in Figs. 4(c)–4(f). Atomic distances (d and h) are in Å, and bond angles (α) are in degrees.

TM	d^1	d^2	d^3	α^1	α^2	α^3	h
Bi-int							
Fe	2.63	3.26	2.40	93.40	79.18	119.65	0.92
Mn	2.82	3.80	2.52	111.30	66.48	107.58	0.10
Cr	2.82	3.61	2.50	105.71	70.49	112.95	0.31
Co	2.57	3.20	2.36	91.72	80.66	119.91	1.04
Ni	2.59	3.03	2.39	87.11	85.73	119.75	1.19
Se-int							
Fe	2.24	2.68	3.55	116.30	78.76	93.69	1.72
Mn	2.43	2.88	3.21	107.53	68.65	103.77	1.38
Cr	2.20	2.74	3.73	118.24	82.32	90.64	1.83
Co	2.32	2.71	3.35	112.37	73.61	98.77	1.55
Ni	2.50	2.73	2.55	106.40	67.61	105.34	1.46

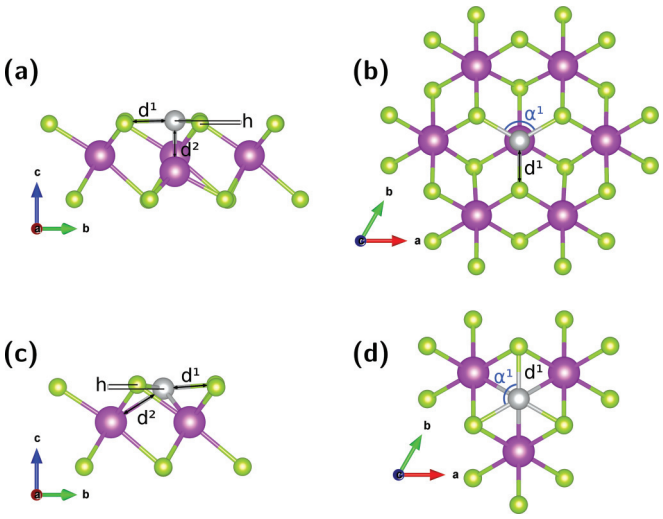

FIG. 5. (Color online) Details of TM adsorbed structures: Bi-ads, side view (a) and top view (b); and Se-ads, side view (c) and top view (d).

configuration we can verify that the Fe ↔ Bi interaction has been strengthened, compared with the former geometry (Bi-ads). Therefore, we can infer the following scenario for Fe adatoms on Bi_2Se_3(111): (i) At low temperatures, the Fe adatom will lie on the Bi_2Se_3(111) surface; this is the Bi-ads geometry. (ii) By increasing the Fe deposition temperature, allowing Fe segregation into the Bi_2Se_3surface, we may have the presence of interstitial Fe atoms (Bi-int). However, for iron deposition at higher temperatures the formation of (energetically most stable) substitutional Fe_{Bi} (Bi-sub) is expected. In this case, there are no Fe-Bi chemical bonds, namely, the Fe ↔ Bi interaction will be weakened. At the equilibrium geometry, the Fe adatom lies nearly at the same plane as the topmost Se atoms, with Fe-Se bond lengths (d^1) of 2.41 and 2.43 Å for the Bi-ads and Se-ads geometries, respectively, where the adsorbed geometries present a c_{3v} symmetry (Fig. 5). In Table IV we summarize the equilibrium geometry of Bi-ads and Se-ads configurations.

TABLE IV. Equilibrium geometry of the adsorbed TM, Bi-ads, and Se-ads configurations, detailed in Figs. 5(a)–5(d). Atomic distances (d and h) are in Å, and bond angles (α) are in degrees.

TM	d^1	d^2	α^1	h
Bi-ads				
Fe	2.41	2.52	119.57	0.28
Mn	2.48	2.68	118.79	0.27
Cr	2.53	2.87	109.25	0.85
Co	2.37	2.46	119.95	0.06
Ni	2.35	2.42	119.98	0.03
Se-ads				
Fe	2.43	2.84	119.40	−0.19
Mn	2.44	3.12	119.46	0.18
Cr	2.39	2.91	118.48	−0.29
Co	2.37	2.87	119.57	−0.16
Ni	2.38	2.82	119.42	−0.18

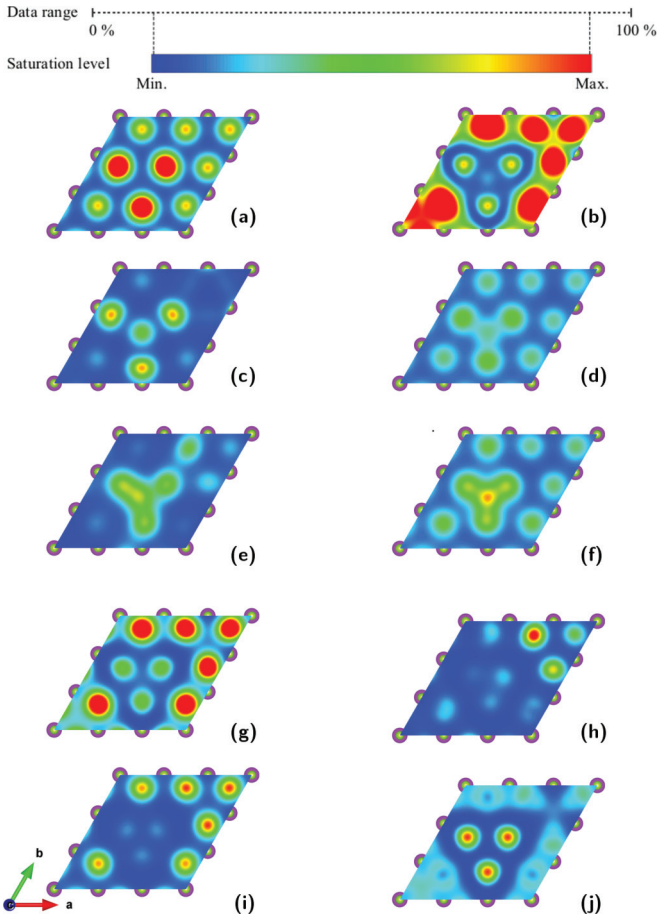

FIG. 6. (Color online) Simulated STM images for occupied (a), (c), (e), (g), (i) and empty (b), (d), (f), (h), (j) states of substitutional Fe_{Bi} (a), (b), interstitial Fe Bi-int (c), (d), adsorbed Fe Bi-ads (e), (f), substitutional Mn_{Bi} (g), (h), and Cr_{Bi} (i), (j). Occupied and empty states are calculated within an energy interval of $E_F \pm 0.3$ eV.

Those different geometries for Fe impurities in Bi_2Se_3(111) will promote different pictures for the charge density distribution on the Fe/Bi_2Se_3(111) surface. In Figs. 6(a) and 6(b) we present the simulated STM images of Bi-sub within an energy interval of 0.3 eV with respect to the Fermi level ($E_F \pm 0.3$ eV). Since the Fe_{Bi}-Se equilibrium bond lengths are shorter than the Bi-Se bond lengths (∼3 Å), the surface Se atoms, attached to the Fe_{Bi} impurity, move downward by 0.28 Å with respect to the other surface Se atoms. Such a structural modification has been identified in our simulated STM images. We verify the formation of a triangular spot lying on the topmost Se atoms above the Fe_{Bi} substitutional atom. It is worth noting that for the occupied states [Fig. 6(a)], the triangular spot is brighter, despite the downward displacement of the surface Se atoms, thus indicating an increase in the occupied electronic density of states, within $E_F - 0.3$ eV, on the (surface) Se atoms neighboring the Fe_{Bi} impurity. In contrast, we find a dark triangular region for the STM images of the empty states [Fig. 6(b)]. Our simulated STM results compare very well with those obtained for Fe/Bi_2Te_3(111).[52] Further STM simulations show that the Bi-int and Bi-ads configurations in Fe/Bi_2Se_3(111) present different pictures for the surface electronic charge density. For interstitial Fe atoms,

Bi-int, we observe a triangular symmetric bright spot on the three Se surface atoms, with an additional central spot on the second-layer Bi atom [Figs. 6(c) and 6(d)]. As described above, in the Bi-int geometry, the interstitial Fe atoms form a $(\text{Fe-Bi})_{\text{split}}$ structure, giving rise to an upward displacement of the second-layer Bi atom. Finally, in Figs. 6(e) and 6(f) we present the STM images of Bi-ads geometry for Fe adatoms on $Bi_2Se_3(111)$. The presence of Fe adatoms can be identified by the formation of a central bright spot on the Fe adatom and the nearest-neighbor surface Se atoms. However, differently from the previous STM images, here we have asymmetric images due to the energetically stable in-plane net magnetic moment ($\langle \mathbf{S} \rangle$), which is discussed in the next section.

Our formation energy results (Table I) show that $\text{Mn}/Bi_2Se_3(111)$ and $\text{Cr}/Bi_2Se_3(111)$ systems present similar behavior compared with $\text{Fe}/Bi_2Se_3(111)$. For both TMs, Bi-sub exhibits the lowest formation energy, followed by Bi-int. Recent experimental results, based on STM images, indicate the formation of substitutional Mn_{Bi} below the topmost Se atoms of $Bi_2Se_3(111)$,[16,20] as well as in $Bi_2Te_3(111)$.[31] There are no Mn-Bi chemical bonds for the Bi-sub geometry. In this case, the Mn_{Bi} atom forms six Mn-Se bonds, with d_{MnSe} values of 2.60 and 2.70 Å, with the top-layer and third-layer Se atoms, respectively, indicated as d^1 and d^2 in Figs. 4(a) and 4(b). Since Mn-Se bonds are shorter than Bi-Se bonds, the three topmost Se atoms (attached to the substitutional Mn_{Bi}) move downward by 0.31 Å. Such a local structural modification can be detected through STM simulations. Figures 6(g) and 6(h) present our STM pictures within an energy interval of $E_F \pm 0.3$ eV. We find a triangular spot lying on the topmost Se atoms bonded to the Mn_{Bi} impurity, for both occupied and empty states. Here, differently from Fe_{Bi} atoms in $\text{Fe}/Bi_2Se_3(111)$ [Figs. 6(a) and 6(b)], the triangular spot is dimmed compared with the rest of the surface Se atoms. In $\text{Cr}/Bi_2Se_3(111)$, the formation of Bi-sub Cr_{Bi}, below the topmost Se atoms, is an exothermic process, $E_F = -0.10$ eV, even under the Bi-rich condition. Indeed, in Ref. 51 the authors also obtained a negative value of E_F for Cr_{Bi} in bulk Bi_2Se_3, while the formation of substitional Cr_{Bi} in $Bi_2Se_3(111)$ has been verified in recent experimental investigations.[22,23] As reported in Table I, the other substitutional (Cr_{Se}), interstitial, and adsorbed configurations are quite unlikely compared with Bi-sub. Thus, we can infer a high concentration of substitutional Cr_{Bi} in $\text{Cr}/Bi_2Se_3(111)$. At the equilibrium geometry, we find three Cr-Se bonds with the topmost Se atoms ($d^1 = 2.54$ Å) and three Cr-Se bonds with the third-layer Se atoms ($d^2 = 2.65$ Å). Similarly to Fe_{Bi} and Mn_{Bi}, there is (somewhat) a local octahedral symmetry around the Cr_{Bi} atom. The surface Se atoms, bonded to Cr_{Bi}, moves downward by 0.35 Å. In Figs. 6(i) and 6(j), through STM simulations, we map the changes in the surface electronic charge density due to the presence of Cr_{Bi} on the $Bi_2Se_3(111)$ surface. For occupied states, we find a dimmed triangular spot on the surface Se atoms above the Cr_{Bi} impurity [Figs. 6(i)], similar to Mn_{Bi}. For empty states, the Se atoms of the triangular spot become brighter compared with the other Se surface atoms [Figs. 6(j)]. This STM pattern is opposite to that observed for Fe_{Bi} impurity.

Finally, we examine the $\text{Co}/Bi_2Se_3(111)$ and $\text{Ni}/Bi_2Se_3(111)$ systems. As indicated in Table I, the formation of substitutional (Bi-sub) impurities is quite unlikely in a Bi-rich environment ($\mu_{\text{Bi}} = \mu_{\text{Bi}}^{\text{max}}$). We find an E^F of 1.69 and 1.33 V for Co_{Bi} and Ni_{Bi}, respectively. On the other hand, at the Bi-poor limit ($\mu_{\text{Bi}} = \mu_{\text{Bi}}^{\text{min}}$), the formation of Co_{Bi} becomes energetically favorable, $E^F = 1.00$ eV, followed by Bi-int ($E^F = 1.14$ eV). Similarly for Ni_{Bi}, its formation energy decreases to 0.65 eV for $\mu_{\text{Bi}} = \mu_{\text{Bi}}^{\text{min}}$. In this case, the Bi-sub and Bi-int configurations exhibit practically the same formation energy, 0.65 and 0.63 eV, respectively. The equilibrium geometries of the substitutional Co_{Bi} and Ni_{Bi} atoms are somewhat similar to those verified for the other substitutional impurities in $Bi_2Se_3(111)$. The Co_{Bi} (Ni_{Bi}) atom becomes sixfold coordinated with the nearest-neighbor Se atoms, with Co_{Bi}-Se (Ni_{Bi}-Se) bond lengths of 2.49 (2.54) and 2.84 (2.65) Å, with the topmost and third-layer Se atoms, respectively, indicated as d^1 and d^2 in Figs. 4(a) and 4(b). The topmost Se atoms, attached to the Co_{Bi} (Ni_{Bi}) impurities, move downward by 0.32 (0.41) Å compared with the other surface Se atoms. The presence of substitutional Bi-sub impurity atoms can be identified through the formation of triangular spots on the topmost Se atoms. Co_{Bi} substitutional impurities give rise to bright (dimmed) triangular spots for the occupied (empty) states within $E_F - 0.3$ ($E_F + 0.3$) eV [Figs. 7(a) and 7(b)]. However, for the Ni_{Bi} system, the topmost Se atoms bonded to the Ni_{Bi} impurity exhibit a reduction in the electronic density of states within $E_F - 0.3$ eV, giving rise to a dimmed triangular [Fig. 7(c)], while for empty states within $E_F + 0.3$ eV, these Se atoms are characterized by bright triangular spots [Fig. 7(d)].

The formation energies of substitutional (Bi-sub) and interstitial (Bi-int) configurations, for Co and Ni impurities, are comparable only under the Bi-poor condition ($\mu_{\text{Bi}} = \mu_{\text{Bi}}^{\text{min}}$). Meanwhile, near the stoichiometric condition, here defined as $\bar{\mu}_{\text{Bi}} = (\mu_{\text{Bi}}^{\text{max}} + \mu_{\text{Bi}}^{\text{min}})/2$, the formation energy of Co_{Bi} and Ni_{Bi} increases to 1.35 and 0.99 eV, respectively. That is, for $\mu_{\text{Bi}} = \bar{\mu}_{\text{Bi}}$, the energetic preference for the Bi-int configuration will be strengthened. The interstitial Co atoms [Figs. 4(c) and 4(d)], similarly to the interstitial Fe atoms, become sevenfold coordinated, with three Co-Se chemical bonds ($d^3 = 2.36$ Å) with the third-layer Se atoms, three Co-Bi chemical bonds with the Bi atoms of the fourth layer ($d^2 = 3.20$ Å), and a Co-Bi bond perpendicular to the surface, forming a $(\text{Co-Bi})_{\text{split}}$ structure with $d^1 = 2.57$ Å. In this case, there is an upward displacement of the second ML Bi atom by 0.74 Å, and the top-layer Se atoms are also displaced vertically by 0.21 Å. Those structural changes on the top-layer surface atoms are identified in our STM images [Figs. 7(e) and 7(f)]. We find three bright spots, for both occupied and unoccupied states, lying on the surface Se atoms above the interstitial Co site. It is noteworthy that there is a slight asymmetry in the STM picture for the occupied states [Figs. 7(e)], which is related to the in-plane orientation of the net magnetic moment $\langle \mathbf{S} \rangle$. Interstitial Ni atoms present a similar equilibrium geometry compared with interstitial Co atoms; *viz.*, three Ni-Se (Ni-Bi) chemical bonds with $d^3 = 2.39$ Å ($d^2 = 3.03$ Å) and the formation of a $(\text{Ni-Bi})_{\text{split}}$ structure ($d^1 = 2.59$ Å), promoting an upward displacement of the topmost Se atoms. These structural changes are visible in the STM images for occupied states, $E_F - 0.3$ eV [Fig. 7(g)], while for empty states ($E_F + 0.3$ eV), we are not able to identify the presence of interstitial Ni atoms [Fig. 7(h)]. For Ni impurities, the

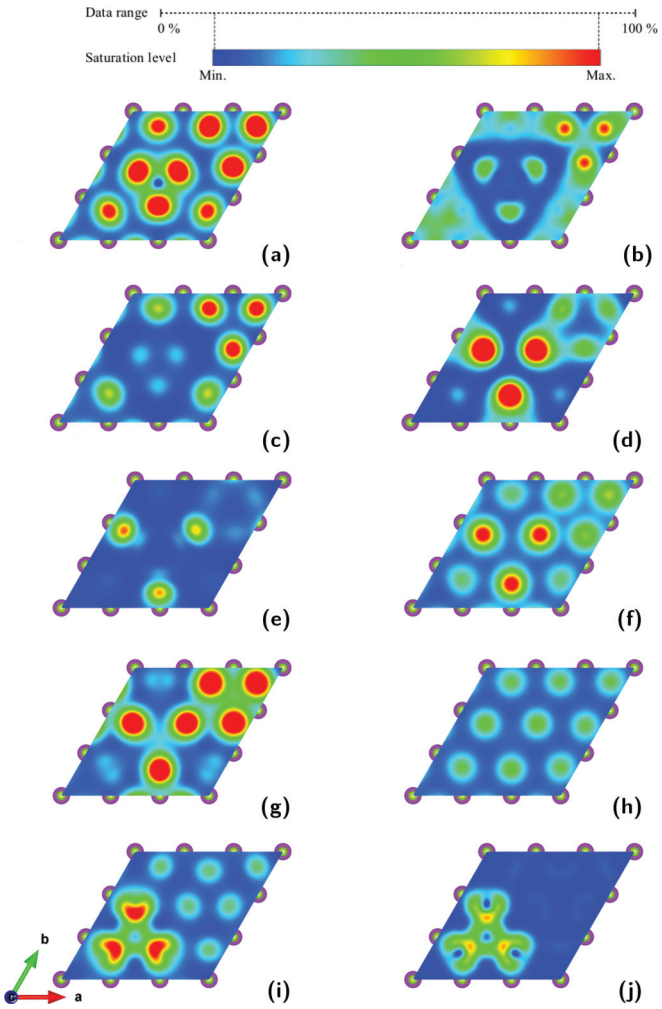

FIG. 7. (Color online) Simulated STM images for occupied (a), (c), (e), (f), (i) and empty (b), (d), (f), (h), (j) states of substitutional Co_{Bi} (a), (b), Ni_{Bi} (c), (d), interstitial Bi-int Co (e), (f), Ni (g), (h), and Se-int Ni (i), (j) impurities in Bi_2Se_3(111). Occupied and empty states are calculated within the energy interval of $E_F \pm 0.3$ eV. Remember that for Se substitutinal sites, the figure is shifted from the origin.

Bi-int and Se-ads geometries are very close in energy (within 50 meV) but present quite different STM patterns, as shown in Figs. 7(g)–7(j). Thus, we can infer the presence of Ni adatoms on the Bi_2Se_3(111) surface (Se-ads), followed by their segregation toward the Bi-int interstitial sites. Similarly for the Co impurities, where the Bi-ads configuration is the second most stable geometry for Co/Bi_2Se_3(111). That is, we may find Co adatoms on the Bi_2Se_3(111) surface. Very recently, the formation of Co/Bi_2Se_3(111) with Co adatoms sitting on the topmost Se atoms has been proposed.[53] However, our formation energy results indicate that such a configuration is quite unlikely. We obtained a formation energy of 3.53 eV, far higher than that of other configurations (see Table I), with the Co adatom lying at 2.26 Å above the topmost Se atom.

C. Topological character of TM/Bi_2Se_3(111)

In order to verify the changes in the electronic properties of the Bi_2Se_3(111) surface in the presence of TM impurities, we examine the electronic band structure and the (Cartesian) components of the SPDOS, $P_\alpha(E)$, projected on the two topmost MLs of TM/Bi_2Se_3(111) systems. The preferential orientation of the spin polarization vector was obtained by comparing the total energies of in-plane ($\langle \mathbf{S}_x \rangle$, $\langle \mathbf{S}_y \rangle$) and out-of-plane ($\langle \mathbf{S}_z \rangle$) orientations of $\langle \mathbf{S} \rangle$. It is noteworthy that, due to the periodic boundary conditions within our supercell approach (composed by a single TM per surface unit cell), our TM/Bi_2Se_3(111) systems are always ferromagnetic.

The substitutional Fe_{Bi}-3*d* orbital gives rise to three (dispersionless) unoccupied bands lying at $\sim(E_F + 0.3)$ eV, depicted by (blue) squares in Fig. 8(a). It is noticeable that the lowest empty Fe_{Bi}-3*d* state hybridizes with the topmost Bi_2Se_3(111) surface atoms at around $E_F + 0.25$ eV, contributing to the formation of the Dirac cone. However, below $E_F + 0.20$ eV, this contribution decreases (<10%), while the two topmost MLs of the Bi_2Se_3(111) surface [(red) circles in Fig. 8] rule the formation of the Dirac cone. We find the small energy gap of 15 meV at the DP. The SPDOS calculations reveal that the Fe/Bi_2Se_3(111) system presents a net spin polarization out of plane for wave vectors along the $\bar{\Gamma}$–$\bar{K}$ and $\bar{\Gamma}$–$\bar{M}$ directions, mainly mediated by the Fe_{Bi}-3*d* impurity orbital, namely, $\langle \varphi_{Fe}(\mathbf{k})|\mathbf{S}|\varphi_{Fe}(\mathbf{k})\rangle \approx \langle \mathbf{S_z} \rangle$ [black lines in Fig. 8(c)], and thus removing the TRS. In addition, as indicated by red lines in Fig. 8(c), the topmost two MLs of Bi_2Se_3(111) also contribute to $\langle \mathbf{S_z} \rangle$ along the $\bar{\Gamma}$–$\bar{K}$ and $\bar{\Gamma}$–$\bar{M}$ directions. On the other hand, near the Fermi level, the SPDOS values of the in-plane components ($\langle \mathbf{S_x} \rangle$ and $\langle \mathbf{S_y} \rangle$) are similar to those obtained for pristine Bi_2Se_3(111) [Fig. 2(c)]. In this case, the Fe_{Bi} contribution is quite negligible.

For the Bi-int configuration we find a metallic band structure [Fig. 8(b)], where partially occupied states are composed by Fe-3*d* orbitals hybridized with surface Se-4*p*. The helical spin texture, as observed for pristine Bi_2Se_3(111), has been suppressed due to the net out-of-plane spin polarization of the Fe impurity along the $\bar{\Gamma}$–$\bar{K}$ and $\bar{\Gamma}$–$\bar{M}$ directions [Fig. 8(d)]. Here, similar to the Bi-sub configuration, the TRS has been suppressed, and there is a downward shift of the surface conduction band. These findings are in agreement with recent experimental measurements,[18,19] while in Ref. 17 the gapless Dirac crossing point has been preserved for Fe coverage up to 0.3 ML. For low coverage of Fe adatoms (0.01 ML), a gapless DP with Fe adatoms lying on the Se-ads site has also been observed.[30] In this case, the absence of an energy gap was attributed to an in-plane net spin polarization of the Fe adatoms. In fact, we find an energetically stable in-plane spin polarization for Fe adatoms, however, not for the Se-ads geometry but for the Bi-ads configuration, which is energetically more stable than Se-ads, by 120 meV (Table I).

Substituional Fe_{Bi} impurities in Bi_2Se_3(111) are electron donors, with ionization state 3^+ and a net magnetic moment (μ) of 5.0 μ_B, while for the interstitial Bi-int, the second most stable configuration, we find an ionization state of between 1^+ and 2^+ and a μ of around 2.5 μ_B. The obtained magnetic moment for Fe_{Bi} is in nice agreement with the recent *ab initio* calculation for substitutional Fe_{Bi} in Bi_2Se_3.[51] In Ref. 18 the authors obtained an ionization state of between 2^+ and 3^+ and a net magnetic moment of around 4 μ_B. Based on a similar calculation approach, West *et al.* obtained 4 μ_B for substituional Fe_{Bi} in Bi_2Te_3(111), while for the interstitial configuration, Bi-int, they obtained $\mu = 4.50$ μ_B.[52]

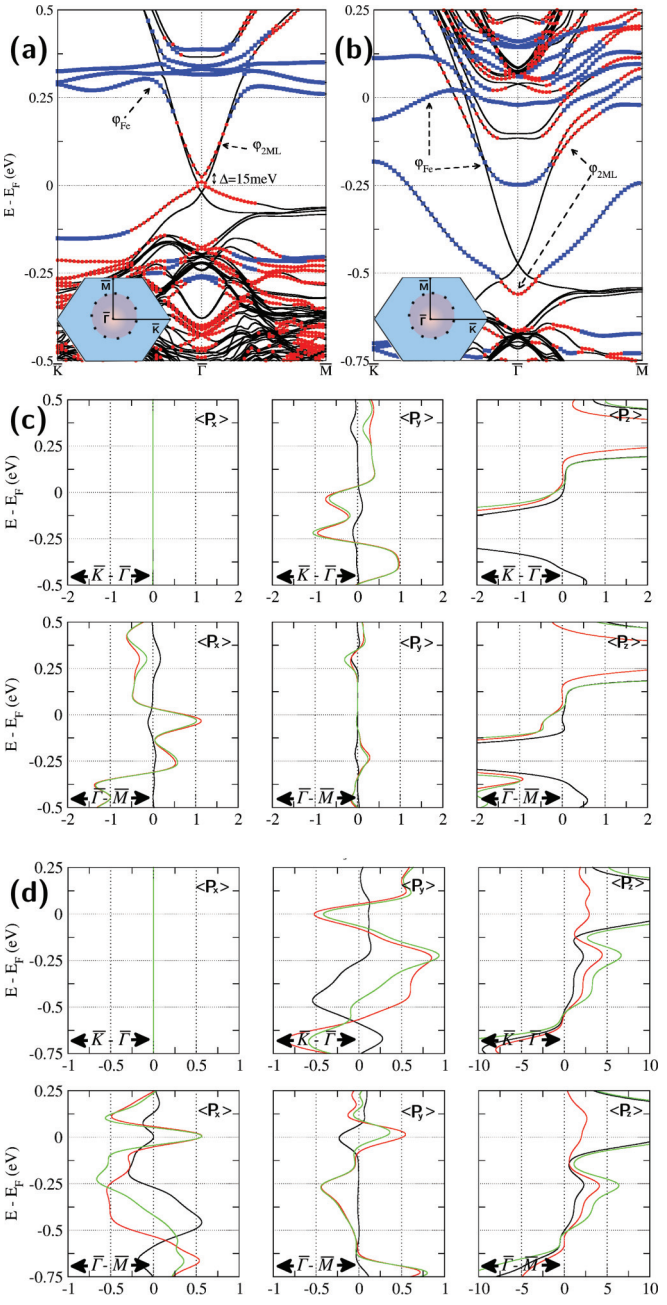

FIG. 8. (Color online) Electronic band structure and SPDOS (in arbitrary units) of Fe/Bi_2Se_3(111) at the substitutional Bi-sub site (a), (c), and interstitial Bi-int site (b), (d). Solid (black) lines in the band structure diagrams (a), (b) indicate the contribution of the whole Fe/Bi_2Se_3(111) slab; (red) circles and (blue) squares indicate the electronic contributions of the topmost two MLs and the Fe impurity, respectively. These contributions were selected by considering a critical percentage (>10%) for the single-particle wave functions of the topmost two MLs and the Fe impurity. The SPDOS (c), (d) projected onto the Fe impurity is indicated by black lines; in red, we have the SPDOS projected on the first two MLs of the Bi_2Se_3(111) surface, excluding the impurity atom; and in green, the sum of the two.

For Fe-adsorbed Bi_2Se_3(111), the Se-ads geometry, an in-plane magnetic moment of 4 μ_B has been verified,[30] while in Ref. 25 the authors obtained an out-of-plane magnetic moment of $\mu \approx 2.9\ \mu_B$ for the Bi-ads configuration.

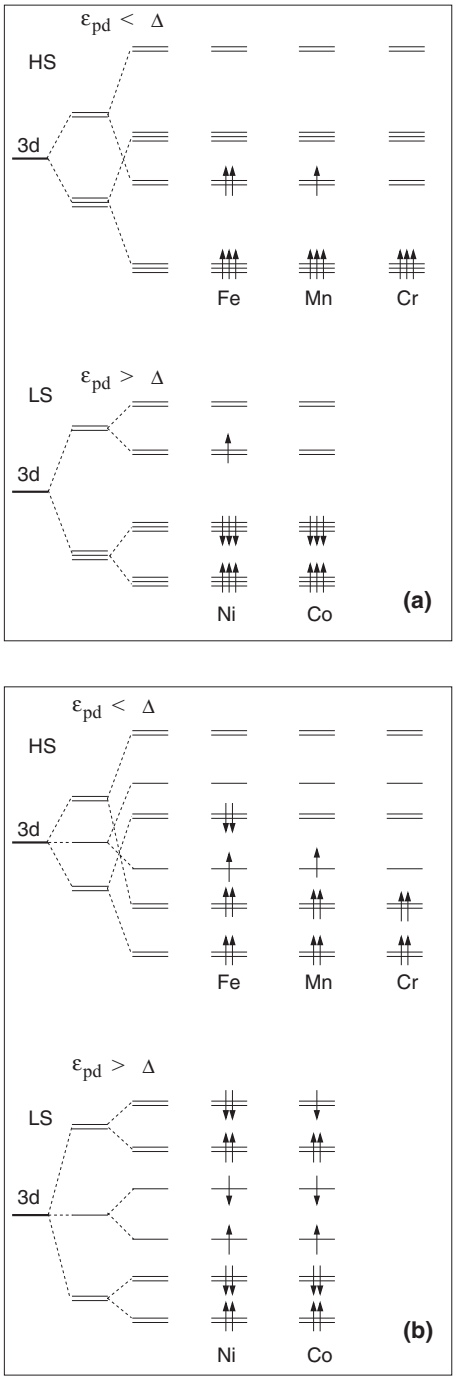

FIG. 9. Energy levels of the 3*d* orbitals of substitutional Bi-sub (a) and interstitial Bi-int (b) TM in Bi_2Se_3(111). HS, high-spin configuration; LS, low-spin configuration.

From the findings described above, we can infer that the chemical interactions between the TM (impurities) and the Bi_2Se_3(111) surface (host) play a fundamental role in the electronic and magnetic properties of TM/Bi_2Se_3(111). In order to provide a clear understanding of the environmental effects on the net magnetic moment of TM impurities, here we examine the energy level splittings of TM-3*d* orbitals embedded in Bi_2Se_3(111). For the substitutional Bi-sub configuration [Fig. 9(a)], the TM exhibits a local octahedral symmetry, giving rise to threefold (*t*) and twofold (*e*) degenerated orbitals.

This energy splitting (ϵ_{pd}) is due to the crystal field induced by the interaction between the (substitutional) TM-3d and the nearest-neighbor (host) Se-4p orbitals. By turning on the spin polarization, further energy splitting takes place due to the exchange field (Δ). In this case, we may have a high-spin configuration for $\epsilon_{pd} < \Delta$, [Fig. 9(a), top], while in Fig. 9(a), bottom, we have the low-spin configuration, $\epsilon_{pd} > \Delta$. Within this scenario, and based on the calculated net magnetic moment of 5.0, 4.0, and 3.0 μ_B for Fe_{Bi}, Mn_{Bi}, and Cr_{Bi}, respectively, we can conclude that those impurities present a high-spin configuration. However, for the Co_{Bi} and Ni_{Bi} substitutional impurities we calculate $\mu = 0.0$ and 1.0 μ_B, respectively, thus matching nicely with the low-spin configuration depicted in Fig. 9(a), bottom. In Table V we summarize our results on the net magnetic moment and the respective (energetically) most likely orientation, i.e., in plane (→) or out of plane (↑).

TABLE V. Magnetic moments (in μ_B) and the energetically most favorable orientations of the net spin polarization, out of plane (↑) or in plane (→), for TM/Bi_2Se_3(111).

Configuration	Cr	Mn	Fe	Co	Ni
Bi-sub	3.0↑	4.0→	5.0↑	0.0×	1.0→
Se-sub	4.0→	3.0↑	2.0→	1.0→	0.0×
Bi-int	4.0→	5.0↑	2.5↑	1.5→	0.0×
Se-int	0.5→	4.0→	2.0→	1.5→	0.0×
Bi-ads	5.0↑	4.0→	2.5→	1.5↑	0.1→
Se-ads	0.4→	4.0↑	2.0↑	1.3↑	0.0×

Similarly to the substitutional Fe_{Bi} impurities, Mn_{Bi} and Cr_{Bi} impurities also induce a small energy gap at the DP, 4 meV [Fig. 10(a)] and 8 meV [Fig. 11(a)], respectively, and the magnetic moments are equal to 4.0 and 3.0 μ_B, respectively. For both systems, the 3d orbitals of the impurities hybridize with the surface states that compose the Dirac cone, whereas far from the center of the Brillouin zone, the impurity states become flat; namely, the localized character of the impurity 3d orbitals is strengthened near the edge of the Brillouin zone. Our SPDOS calculations [Figs. 10(c) and 11(b)] confirm this impurity ↔ surface hybridization. For Mn_{Bi}/Bi_2Se_3(111) there is an energetic preference for the in-plane orientation (Table V), where the impurity states and the electronic states

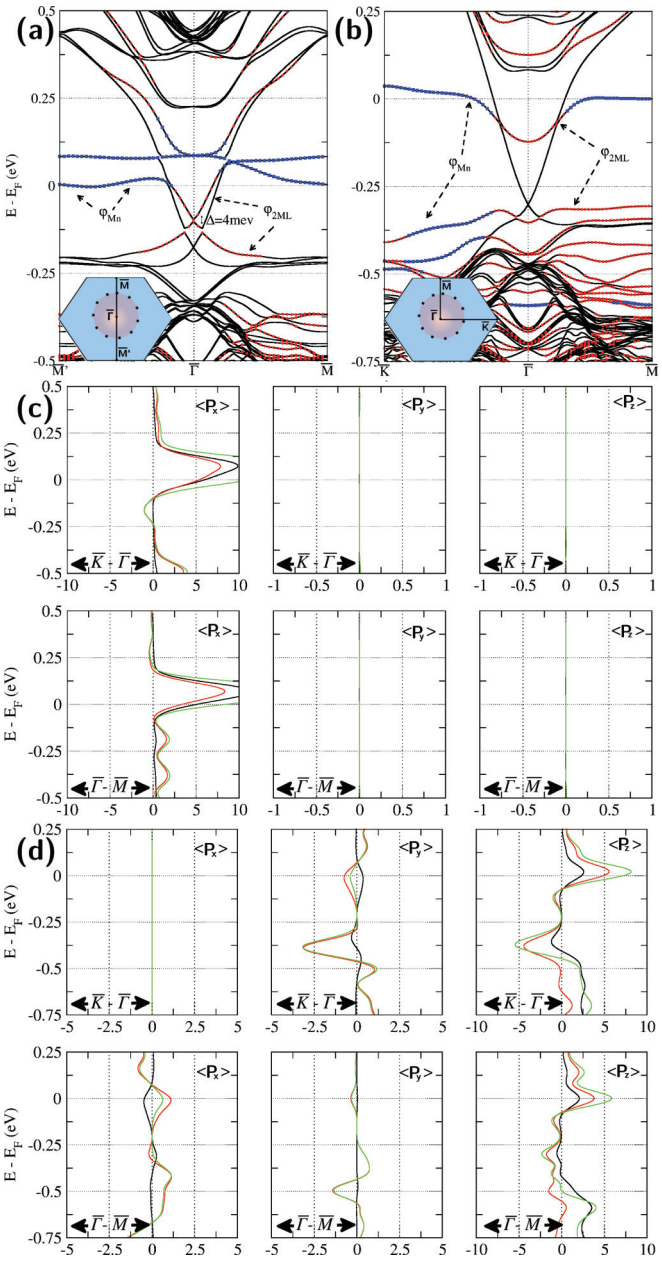

FIG. 10. (Color online) Same as Fig. 8, for substitutional Mn_{Bi} (a), (c) and interstitial Mn Bi-int (b), (d).

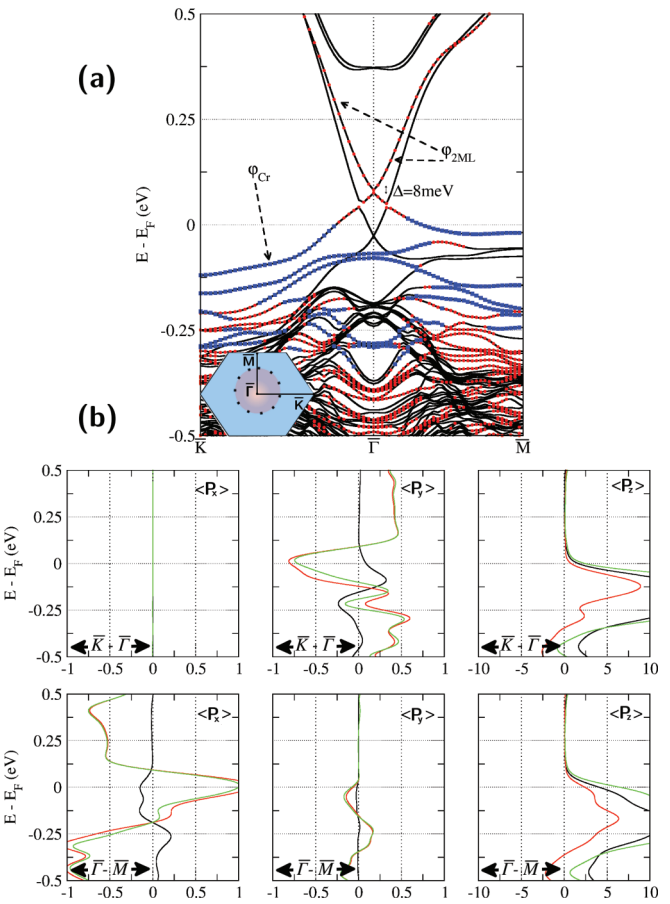

FIG. 11. (Color online) Same as Fig. 8, for substitutional Cr_{Bi}.

of the two topmost MLs of the $Bi_2Se_3(111)$ contribute to the net magnetic moment, $\langle\varphi_{2ML}(\mathbf{k})|\mathbf{S}|\varphi_{2ML}(\mathbf{k})\rangle = \langle\mathbf{S}_x\rangle$ in Fig. 10(c), while the other components of the spin polarization vector, $\langle\mathbf{S}_y\rangle$ and $\langle\mathbf{S}_z\rangle$, are suppressed. However, for $Cr_{Bi}/Bi_2Se_3(111)$ we find the out-of-plane $\langle\mathbf{S}_z\rangle$ configuration to be the energetically more stable [Fig. 11(b)]. The calculated magnetic moment for Cr_{Bi}, 3.0 μ_B out of plane, compares very well with recent experimental findings[22] and theoretical *ab initio* calculations.[51]

The presence of a small energy gap at the DP, around 7 meV, has been experimentally observed for (ferromagnetic) Mn-doped $Bi_2Se_3(111)$.[19] Further experimental investigations confirm the formation of an energy gap at the DP, breaking the TRS, indicating the presence of substitutional Mn_{Bi}.[16] In the latter work, the authors also verified a ferromagnetic phase for $Mn_{Bi}/Bi_2Se_3(111)$, with a net magnetic moment of $\sim$3.45 μ_B. However, due to the inhomogeneous distribution of Mn impurities embedded in the $Bi_2Se_3(111)$ host (giving rise to a "spatially dependent magnetic field"), they find both out-of-plane and in-plane orientations for the net magnetic moment.[16] Very recently, a "hedgehog" -like spin texture, breaking the TRS, has been proposed for $Mn/Bi_2Se_3(111)$, where there is a combination of in-plane and out-of-plane magnetic moments.[20] Our results of magnetic moments indeed indicate that there is a dependence between the (local) configuration of the Mn impurity and the preferential orientation of its magnetic moment $\langle\mathbf{S}\rangle$ (see Table V). That is, for the energetically most stable configuration, Mn_{Bi}, $\langle\mathbf{S}\rangle$ is in plane, while for the second most stable configuration, interstitial Bi-int (see Table I), the magnetic moment becomes out of plane, with $\mu = 5.0\ \mu_B$. Figures 10(b) and 10(d) present the electronic band structure and the SPDOS for the Bi-int configuration for $Mn/Bi_2Se_3(111)$. The DP has been suppressed [Fig. 10(b)], where we find a partially occupied Mn-3d band within the energy gap of Bi_2Se_3, and the helical spin texture has been removed due to the out-of-plane $\langle\mathbf{S}_z\rangle$ spin component [Fig. 10(d)]. For the other interstitial geometry, Se-int, the Mn impurity exhibits an in-plane magnetic moment of 4.0 μ_B. The formation energies of Mn adsorbed systems, Bi-ads and Se-ads, are very close ($E^F = 0.74$ and 0.87 eV, respectively), and for both configurations we find a net magnetic moment of 4.0 μ_B, however, it is in plane for Bi-ads and out of plane for Se-ads. Those findings support the spatial dependence of the magnetic field in $Mn/Bi_2Se_3(111)$.[16]

The local symmetry of the most likely configuration for Co and Ni in $Bi_2Se_3(111)$, Bi-int, is different compared with the substitutional Bi-sub. For the Bi-int configuration the local symmetry around the impurity atom is close to C_{3v}, where the orbital splittings, for high-spin and low-spin systems, are depicted in Figs. 9(b), top and bottom, respectively. Both impurities present a low-spin configuration ($\epsilon_{pd} > \Delta$) and magnetic moments of 1.5 and 0.0 μ_B, for Co and Ni, respectively.

Upon the presence of interstitial Co atoms (Bi-int) the $Co/Bi_2Se_3(111)$ surface becomes metallic [Fig. 12(a)]. Figure 12(c) presents the SPDOS projected onto the Co impurity and the topmost two MLs of the $Bi_2Se_3(111)$ surface. We find an energetic preference for an in-plane magnetic moment, $\langle\mathbf{S}_x\rangle$, along the $\bar{\Gamma}$–$\bar{M}$ and $\bar{\Gamma}$–$\bar{K}$ directions, ruled by the Co impurity and the (topmost) surface atoms of $Bi_2Se_3(111)$. Similarly

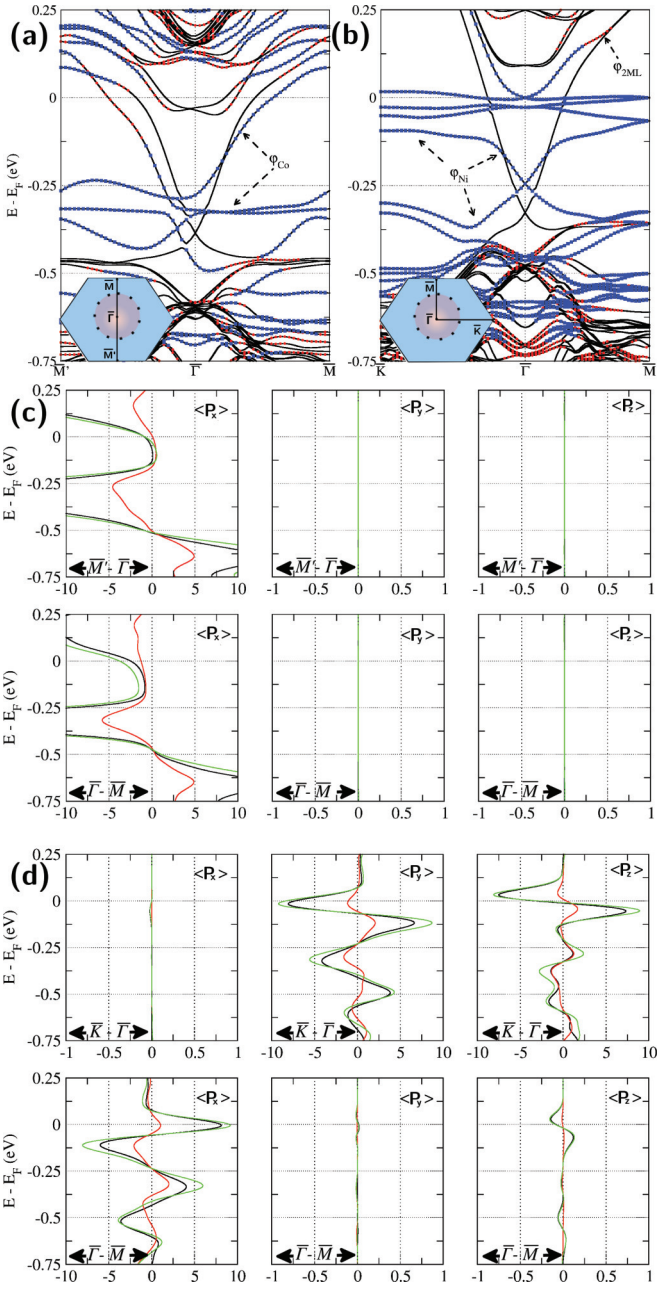

FIG. 12. (Color online) Same as Fig. 8, for Co interstitial Bi-int (a), (c) and $Ni/Bi_2Se_3(111)$ (b), (d).

to the $Mn_{Bi}/Bi_2Se_3(111)$ system, the other components of $\langle\mathbf{S}\rangle$ are suppressed, as well as the helical spin texture of the system. The net magnetic moment of the Co impurity also depends on the local environment within the Bi_2Se_3 host. For instance, as reported in Tables I and V, the adsorbed geometries (Bi-ads and Se-ads) are the second most likely configurations for $Co/Bi_2Se_3(111)$, and for these geometries we find an energetic preference for out-of-plane spin polarization, whereas for the other interstitial geometry, Se-int, we find an in-plane magnetic moment. In contrast, the gapless DP has been preserved for interstitial Bi-int Ni impurities [Fig. 12(b)]. The DP lies at $E_F - 0.25$ eV, indicating an electron donor character for the interstitial Ni atoms. There is a clear contribution from the Ni-3d orbitals to the formation of the Dirac cone. Here,

differently from the other TM/Bi_2Se_3(111) systems, the helical character of the spin polarization vector has been preserved [Fig. 12(d)], where the impurity Ni atom dominates the SPDOS along the $\bar{\Gamma}$–$\bar{M}$ and $\bar{\Gamma}$–$\bar{K}$ directions.

IV. SUMMARY

In summary, based on *ab initio* calculations, we provide a comprehensive map of the energetic stability and the electronic properties of the TM-doped Bi_2Se_3(111) TI. Initially, ruled by the formation energy results, the most likely configurations of TMs in Bi_2Se_3(111) have been identified as (i) substitutional (Bi-sub) for Cr, Mn, and Fe atoms, even under the Bi-rich condition. (ii) At the Bi-poor limit, the Co and Ni impurities also exhibit an energetic preference for the Bi substitutional sites. However, (iii) near the stoichiometric condition, the interstitial configuration (Bi-int) becomes energetically more favorable for Co and Ni. In addition, for Fe and Mn atoms, there are other configurations somewhat close in energy, namely, interstitial Bi-int and adsorbed (Bi-ads and Se-ads) configurations, thus suggesting a variety of different environments for Fe and Mn impurities embedded in Bi_2Se_3(111). Similarly for Co/Bi_2Se_3(111) and Ni/Bi_2Se_3(111), where the adsorbed geometries are also energetically close to the Bi-int configuration. In contrast, the same variety of possible geometries is not expected for Cr. The electronic properties of the topologically protected surface states change dramatically in the presence of TMs. Indeed, our simulated STM results indicate that each TM/Bi_2Se_3(111) system exhibits a particular surface electronic picture as a function of the TM atomic species and its equilibrium geometry. Further detailed electronic band structure investigations reveal that substitutional Fe_{Bi} and Cr_{Bi} impurities present a net spin polarization out of plane, giving rise to a small energy gap at the DP. Meanwhile, the spin polarization is in plane for Mn_{Bi}, also giving rise to a small energy gap at the DP. In general, for substitutional impurities, the shape of the Dirac cone is preserved compared with the pristine Bi_2Se_3(111) surface. However, except for Ni/Bi_2Se_3(111), these surface states are no longer topologically protected, since the TRS has been removed. Interstitial Bi-int Co impurities also present an in-plane spin polarization, however, it becomes out of plane for the (energetically close) adsorbed geometry. Indeed, this commitment between the local geometry and the electronic properties has been verified for other TM/Bi_2Se_3(111) systems. For instance, for Fe and Mn adatoms, we may have in-plane or out-of-plane spin polarizations depending on the adsorption sites, namely Bi-ads or Se-ads (see Table V).

ACKNOWLEDGMENTS

The authors acknowledge financial support from the Brazilian agencies CNPq, FAPESP, and FAPEMIG and thank the CENAPAD-SP for computer time.

*leonabdalla@gmail.com
†hiroki@infis.ufu.br

[1] M. Hasan and C. Kane, Rev. Mod. Phys. **82**, 3045 (2010).
[2] T. Fukui, T. Fujiwara, and Y. Hatsugai, J. Phys. Soc. Jpn. **77**, 123705 (2008).
[3] R. Resta and D. Vanderbilt, Phys. Ferroelec. **68**, 31 (2007).
[4] J. Moore and L. Balents, Phys. Rev. B **75**, 121306 (2007).
[5] L. Fu and C. Kane, Phys. Rev. B **74**, 195312 (2006).
[6] C. L. Kane and E. J. Mele, Phys. Rev. Lett. **95**, 146802 (2005).
[7] B. A. Bernevig and S. C. Z. T. L. Hughes, Science **314**, 1757 (2006).
[8] M. König, S. Wiedmann, C. Brüne, A. Roth, H. Buhmann, L. W. Molenkamp, X.-L. Qi, and S.-C. Zhang, Science **318**, 766 (2007).
[9] H. Zhang, C.-X. Liu, X.-L. Qi, X. Dai, Z. Fang, and S.-C. Zhang, Nature Phys. **5**, 438 (2009).
[10] W. Zhang, R. Yu, H.-J. Zhang, X. Dai, and Z. Fang, New J. Phys. **12**, 065013 (2010).
[11] D. Hsieh, Y. Xia, D. Qian, L. Wray, J. H. Dil, F. Meier, J. Osterwalder, L. Patthey, J. G. Checkelsky, N. P. Ong, A. V. Fedorov *et al.*, Nature **460**, 1101 (2009).
[12] X.-L. Qi and S.-C. Zhang, Rev. Mod. Phys. **83**, 1057 (2011).
[13] Y.-L. Wang, Y. Xu, Y.-P. Jiang, J.-W. Liu, C.-Z. Chang, M. Chen, Z. Li, C.-L. Song, L.-L. Wang, K. He *et al.*, Phys. Rev. B **84**, 075335 (2011).
[14] Y. S. Hor, P. Rouchan, H. Beidenkopf, J. Seo, D. Qu, J. G. Checkelsky, L. A. Wray, D. Hsieh, Y. Xia, S. Y. Xu, D. Qian, M. Z. Hasan, N. P. Ong, A. Yazdani, and R. J. Cava, Phys. Rev. B **81**, 195203 (2010).
[15] Y. S. Hor, A. J. Williams, J. G. Checkelsky, P. Roushan, J. Seo, Q. Xu, H. W. Zandbergen, A. Yazdani, N. P. Ong, and R. J. Cava, Phys. Rev. Lett. **104**, 057001 (2010).
[16] D. Zhang, A. Richardella, D. W. Rench, S. Y. Xu, A. Kandala T. C. Flanagan, H. Beidenkopf, A. L. Yeats, B. B. Buckley, P. V. Klimov *et al.*, Phys. Rev. B **86**, 205127 (2012).
[17] M. R. Scholz, J. Sánchez-Barriga, D. Marchenko,, A. Varykhalov, A. Volykhov, L. V. Yashina, and O. Rader, Phys. Rev. Lett. **108**, 256810 (2012).
[18] L. A. Wray, S. Xu, Y. Xia, D. Hsieh, A. V. Fedorov, Y. S. Hor, R. J. Cava, A. Bansil, H. Lin, and M. Z. Hasan, Nat. Phys. **7**, 32 (2011).
[19] Y. L. Chen, J. Chu, J. G. Analytis, Z. K. Liu, K. Igarashi, H. Kuo, X. L. Qi, S. K. Mo, R. G. Moore, D. H. Lu *et al.*, Science **329**, 659 (2010).
[20] S. Y. Xu, M. Neupane, C. Liu, D. Zhang, A. Richardella, L. A. Wray, N. Alidoust, M. Leandersson, T. Balasubramanian, J. Sánchez-Barriga *et al.*, Nat. Phys. **8**, 616 (2012).
[21] T. Valla, Z.-H. Pan, D. Gardner, Y. S. Lee, and S. Chu, Phys. Rev. Lett. **108**, 117601 (2012).
[22] P. P. Haazen, J. B. Laloë, T. J. Nummy, H. J. M. Swagten, P. Jarillo-Herrero, D. Heiman, and J. S. Moodera, Appl. Phys. Lett. **100**, 082404 (2012).
[23] Y. H. Choi, N. H. Jo, K. J. Lee, C. Y. You, and M. H. Jung, J. Appl. Phys. **109**, 07E312 (2012).
[24] Q. Liu, C.-X. Liu, C. Xu, X.-L. Qi, and S.-C. Zhang, Phys. Rev. Lett. **102**, 156603 (2009).
[25] Z. L. Li, J. H. Yang, G. H. Chen, M. H. Whangbo, H. J. Xiang, and X. G. Gong, Phys. Rev. B **85**, 054426 (2012).
[26] H. Jin, J. H. Song, and A. J. Freeman, Phys. Rev. B **83**, 125319 (2011).
[27] J. Henk, A. Ernst, S. V. Eremeev, E. V. Chulkov, I. V. Maznichenko, and I. Mertig, Phys. Rev. Lett. **108**, 206801 (2012).
[28] K.-H. Jin and S.-H. Jhi, J. Phys. Condens. Matt. **24**, 175001 (2012).

[29]T. M. Schmidt, R. H. Miwa, and A. Fazzio, Phys. Rev. B **84**, 245418 (2011).
[30]J. Honolka, A. A. Khajetoorians, V. Sessi, T. O. Wehling, S. Stepanow, J. L. Mi, B. B. Iversen, T. Schlenk, J. Wiebe, N. B. Brookes *et al.*, Phys. Rev. Lett. **108**, 256811 (2012).
[31]J. Henk, M. Flieger, I. V. Maznichenko, I. Mertig, A. Ernst, S. V. Eremeev, and E. V. Chulkov, Phys. Rev. Lett. **109**, 076801 (2012).
[32]P. Hohenberg and W. Kohn, Phys. Rev. **136**, B864 (1964).
[33]W. Kohn and L. J. Sham, Phys. Rev. **140**, A1133 (1965).
[34]P. E. Blüchl, Phys. Rev. B **50**, 17953 (1994).
[35]G. Kresse and D. Joubert, Phys. Rev. B **59**, 1758 (1999).
[36]J. P. Perdew, K. Burke, and M. Ernzerhof, Phys. Rev. Lett. **77**, 3865 (1996).
[37]G. Kresse and J. Furthmüller, Phys. Rev. B **54**, 11169 (1996).
[38]O. V. Yazyev, J. E. Moore, and S. G. Louie, Phys. Rev. Lett. **105**, 266806 (2010).
[39]S. B. Zhang and J. E. Northrup, Phys. Rev. Lett. **67**, 2339 (1991).
[40]For the cohesive energy we calculated the total energy of the bulk most common phase per atom and subtracted it from the total energy of the single atom, all with the inclusion of spin-orbit interaction. The Kohn-Sham orbitals in all calculations were expanded in a plane-wave basis set with an energy cutoff of 270 eV. We obtained the following cohesive energies (in eV/atom): Cr, 4.03; Mn, 3.73; Fe, 4.87; Co, 5.27; Ni, 4.46; Bi, 2.16; and Se, 2.58. These are all in excellent agreement with both experiment and theory.
[41]P. H. T. Philipsen and E. J. Baerends, Phys. Rev. B **54**, 5326 (1996).
[42]C. Kittel, *Introduction to Solid State Physics* (John Wiley, New York, 1995).
[43]V. R. Sidoroku, L. V. Goncharuk, and R. V. Antonenko, Powder Metall. Metal Ceram. **4**, 234 (2008).
[44]J. Tersoff and D. R. Hamann, Phys. Rev. B **31**, 805 (1985).
[45]K. Park, J. J. Heremans, V. W. Scarola, and D. Minic, Phys. Rev. Lett. **105**, 186801 (2010).
[46]S. Urazhdin, D. Bilc, S. H. Tessmer, S. D. Mahanti, T. Kyratsi, and M. G. Kanatzidis, Phys. Rev. B **66**, 161306(R) (2002).
[47]B. Yan, D. Zhang, and C. Felser, Phys. Status Solidi RRL **7**, 148 (2013).
[48]Y. A. Bychkov and E. I. Rashba, J. Exp. Theor. Phys. Lett. **39**, 78 (1984).
[49]J. H. Dil, J. Phys. Condens. Matter **21**, 403001 (2009).
[50]Y. Zhang, K. He, C. Chang, C. Song, L. Wang, X. Chen, J. Jia, Z. Fang, X. Dai, W. Shan *et al.*, Nat. Phys. **6**, 584 (2010).
[51]J. M. Zhang, W. Zhu, Y. Zhang, D. Xiao, and Y. Yao, Phys. Rev. Lett. **109**, 266405 (2012).
[52]D. West, Y. Y. Sun, S. B. Zhang, T. Zhang, X. Ma, P. Cheng, Y. Y. Zhang, X. Chen, J. F. Jia, and Q. K. Xue, Phys. Rev. B **85**, 081305(R) (2012).
[53]M. Ye, S. V. Eremeev, K. Kuroda, E. E. Krasovskii, E. V.Chulkov, Y. Takeda, Y. Saitoh, K. Okamoto, S. Y. Zhu, K. Miyamoto *et al.*, Phys. Rev. B **85**, 205317 (2012).